Physica E 42 (2010) 1251–1261

Contents lists available at ScienceDirect

Physica E

journal homepage: www.elsevier.com/locate/physe

Invited Review

Resonance Raman spectroscopy of the radial breathing modes in carbon nanotubes

P.T. Araujo [a], P.B.C. Pesce [a], M.S. Dresselhaus [c,d], K. Sato [e], R. Saito [f], A. Jorio [a,b,*]

[a] Departamento de Física, Universidade Federal de Minas Gerais, Av. Antonio Carlos, 6627, Campus Pampulha, Belo Horizonte, MG 30123-970, Brazil
[b] Divisão de Metrologia de Materiais, Instituto Nacional de Metrologia, Normalização e Qualidade Industrial (INMETRO), Duque de Caxias, RJ 25250-020, Brazil
[c] Department of Electrical Engineering and Computer Science, Massachusetts Institute of Technology, Cambridge, MA 02139-4307, USA
[d] Department of Physics, Massachusetts Institute of Technology, Cambridge, MA 02139-4307, USA
[e] Department of Mechanical Engineering, The University of Tokyo, 7-3-1 Hongo, Bunkyo-ku, Tokyo 113-8656, Japan
[f] Department of Physics, Tohoku University, Sendai 980-8578, Japan

ARTICLE INFO

Article history:
Received 29 December 2009
Accepted 10 January 2010
Available online 18 January 2010

Keywords:
Carbon nanotubes
Dielectric screening
Environmental effects
Transition energies
Radial breathing mode
Raman spectroscopy

ABSTRACT

In the last decade, many theoretical and experimental achievements have been made in the photophysics of single wall carbon nanotubes (SWNTs). Such accomplishments allowed us to gain a deep understanding of the photophysics behind the transition energy (E_{ii}) and the radial breathing mode frequency (ω_{RBM}) dependence on nanotube chirality (n, m). This work is devoted to assemble and discuss what has been done on the research of the SWNT electronic and vibrational properties, based on the radial breathing mode (RBM) resonance Raman spectroscopy. Attention is directed to the understanding of how a change in the environment changes the correlation between (E_{ii}, ω_{RBM}) and (n, m). From the analysis of several data in the literature, we derive a simple routine for the $(E_{ii}, \omega_{RBM}) \rightarrow (n, m)$ assignment.

Contents

1. Introduction

Due to their 1D character, single-walled carbon nanotubes (SWNTs) exhibit unique electronic and vibrational properties that make them an interesting material for technological applications in electronics and optoelectronics [1–8]. Associated with each individual SWNT is a unique pair of indices (n, m) that fingerprints all of its properties [9,10]. Therefore, the knowledge of (n, m) is of great importance for defining the properties and applications for each SWNT [9,10]. Quantum confinement is responsible for the rise of van-Hove singularities in the SWNTs electronic and vibrational density of states resulting in (n, m)-dependent optical properties [9,10]. The most frequently used optically based

* Corresponding author at: Departamento de Física, Universidade Federal de Minas Gerais, Av. Antonio Carlos, 6627, Campus Pampulha, Belo Horizonte, MG 30123-970, Brazil. Tel.: +55 31 34096638; fax: +55 31 34095600.
E-mail address: adojorio@fisica.ufmg.br (A. Jorio).

1386-9477/$ - see front matter © 2010 Elsevier B.V. All rights reserved.
doi:10.1016/j.physe.2010.01.015

Table 1
A and **B** values for the relation $\omega_{RBM} = \mathbf{A}/\mathbf{d_t} + \mathbf{B}$ reported in the literature.

Sample	A	B
Alcohol-assisted CVD SWNTs [11]	217	15
Water-assisted CVD SWNTs [13]	227	0
Laser ablation bundled SWNTs [14]	232	0
SWNTs at silicon substrate [15]	248	0
HiPco SWNTs SDS[a]-dispersed [16]	223.5	12.5
HiPco SWNTs SDS[a]-dispersed [19]	214.4	18.7
HiPco SWNTs SDS[a]-dispersed [21]	218	17
Free-hanging SWNTs [22]	204	27
HiPco SWNTs SDS[a]-dispersed [47]	227	7.3/11.8[b]

[a] SDS stands for sodium dodecyl sulfate.
[b] Different values of **B** were found for semiconducting/metallic SWNTs.

experimental technique to properly assign the (n, m) indices is resonance Raman spectroscopy (RRS). By knowing (1) the SWNT optical transition energies E_{ii} and (2) its radial breathing mode frequency (ω_{RBM}) as measured by RRS, together with their (E_{ii}, ω_{RBM}) changes with a changing environment it is possible to uniquely assign the (n, m) for an individual SWNT [10–21].

The last decade has been marked by an impressive development in understanding the nature of the optical transition energies E_{ii} in quasi-1D SWNTs, where $i = 1, 2, 3, \ldots$ denotes the inter-subband transitions between the i th valence and the i th conduction band for a given SWNT [11–32]. While the interest in the excitonic nature of E_{ii} and the dielectric screening in 1D structures dates back to research in π- conjugated polymers [10], in carbon nanotubes the interest to these topics started in 2003 with the identification of the so-called "ratio problem" [33]. In 2007, Araujo et al. [11] and Michel et al. [12] showed that the scaling law for the exciton energies explaining the "ratio problem" [33] breaks down for transitions with energies greater than E_{11}^{M}.[1] These results led to the discussion of the excitonic nature of the higher energy levels, where quantum-chemistry calculations and solid-state physics (tight-bind and first-principles) calculations give contradictory pictures [11,34] due to a lack of knowledge about the dielectric screening in SWNTs. A large amount of information about the E_{ii} transitions is now available for a large range of tube diameters ($0.7 < d_t < 6$ nm) [11–32],and the E_{ii} for SWNTs are now understood theoretically in terms of the bright exciton energy [10,34,35]. The E_{ii} can now be accurately described by tight-binding calculations, including corrections for curvature optimization and many-body effects [10,33–40], plus an empirically based diameter dependence for the dielectric screening in SWNTs [41].

Parallel to this progress on understanding the E_{ii} in greater detail was the development of the physics behind the radial breathing mode (RBM) frequency (ω_{RBM}). The RBM provides the spectroscopic signature of SWNTs [10,42], and the ω_{RBM} depends on the SWNT diameter (d_t), which is related to the SWNT (n, m) structural indices by $d_t = 0.142\sqrt{3(n^2+mn+m^2)}/\pi$ [10]. The experimental results in the literature have been fitted with the relation $\omega_{RBM} = \mathbf{A}/d_t + \mathbf{B}$, with values for **A** and **B** varying from paper to paper (see Table 1) [11,14–22]. The empirical constant factor **B** prevents the expected limit of a graphene sheet from being achieved, where the ω_{RBM} should go to zero when d_t approaches infinity. Therefore, **B** is supposedly associated with an environmental effect on ω_{RBM}, rather than an intrinsic property of SWNTs. An environmental effect here implies the effect of the surrounding medium, such as bundling, molecules adsorbed from the air, surfactant used for SWNT bundles dispersion, or substrates on which the tubes are sitting. Nowadays, the relation between ω_{RBM} and d_t is described by $\omega_{RBM} = (227/d_t)\sqrt{1 + C_e \cdot d_t^2}$, where C_e is the only adjustable constant that weights the effect of the medium surrounding the SWNTs [13].

This article reviews the experimental efforts made to establish the E_{ii} and ω_{RBM} physics of carbon nanotubes thus making possible a reliable RRS-based (n, m) assignment.

2. The ω_{RBM} vs. d_t relation and the role of a changing environment

Recently, resonance Raman scattering has been used to measure the RBMs of SWNTs grown by the water-assisted chemical vapor deposition (CVD) method [43–46]. This water-assisted CVD process has been called "super-growth" and generates millimeter-long isolated SWNTs of high-purity. The "super-growth" SWNTs exhibit a broad d_t distribution (d_t from 1 to 6 nm) and all tube chiralities ($0^\circ \le \theta \le 30^\circ$). The SWNTs are vertically aligned from a silicon substrate to form a very low density material, where SWNTs represent only 3.6% of the total volume [43–46]. With the "super-growth" sample, 125 Raman spectra, each at a different E_{laser} excitation energy, are used to assign the (n, m) structure of 197 different SWNTs (of which 73 are metallic and 124 semiconducting) [13]. Using all the 197 (n, m) SWNTs assigned and the relation $d_t = 0.142\sqrt{3(n^2+mn+m^2)}/\pi$, the experimental ω_{RBM} can be plotted as a function of d_t, as shown in Fig. 1. Fitting the data shown in Fig. 1 using the relation $\omega_{RBM} = \mathbf{A}/d_t + \mathbf{B}$, the values of the fitting parameters $\mathbf{A} = (227.0 \pm 0.3)\,\mathrm{cm^{-1}\,nm}$ and $\mathbf{B} = (0.3 \pm 0.2)\,\mathrm{cm^{-1}}$ are obtained. Therefore, these SWNTs follow a simple linear relation between ω_{RBM} and d_t, with the proportionality constant $\mathbf{A} = 227.0\,\mathrm{cm^{-1}\,nm}$, in agreement with the elastic properties of graphite [48], and with a negligible environmental effect ($\mathbf{B} \approx 0$). All the observed ω_{RBM} values reported in the literature are upshifted from this fundamental relation [11,14–22].

By gathering most of the results presented in the literature and comparing them with the results obtained for the "super-growth" (*S.G.*) sample, all the $\omega_{RBM}^{Lit.}$ presented in the literature are upshifted with relation to the $\omega_{RBM}^{S.G.}$. Fig. 2(a) shows the difference between several $\omega_{RBM} = \mathbf{A}/d_t + \mathbf{B}$ found in the literature

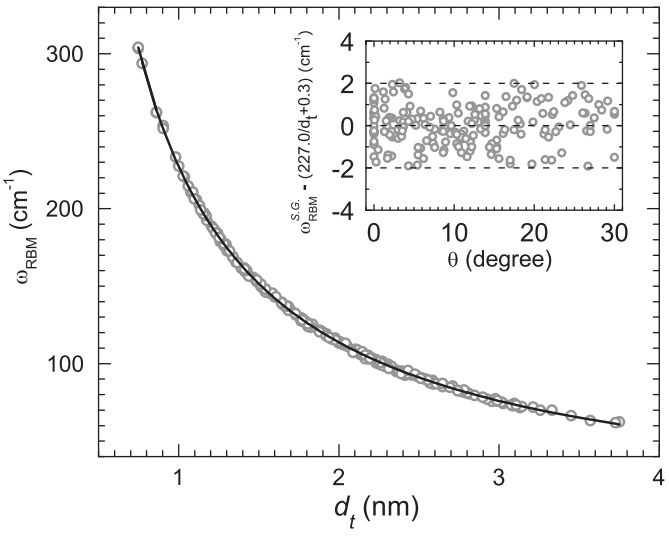

Fig. 1. Experimental radial breathing mode frequency (ω_{RBM}) as a function of tube diameter (d_t). Open circles represent the SWNT $\omega_{RBM}^{S.G.}$ data and the solid line is a fit to the data, given by $\omega_{RBM} = 227.0/d_t + 0.3\,\mathrm{cm^{-1}}$. The inset plots the difference between the experimental ω_{RBM} and $227.0/d_t + 0.3\,\mathrm{cm^{-1}}$ as a function of SWNT chiral angle (θ) [13].

[1] The superscripts of $E_{ii}^{S,M}$ for $i = 1, 2, 3, \ldots$ stand, respectively, for semiconducting and metallic SWNTs.

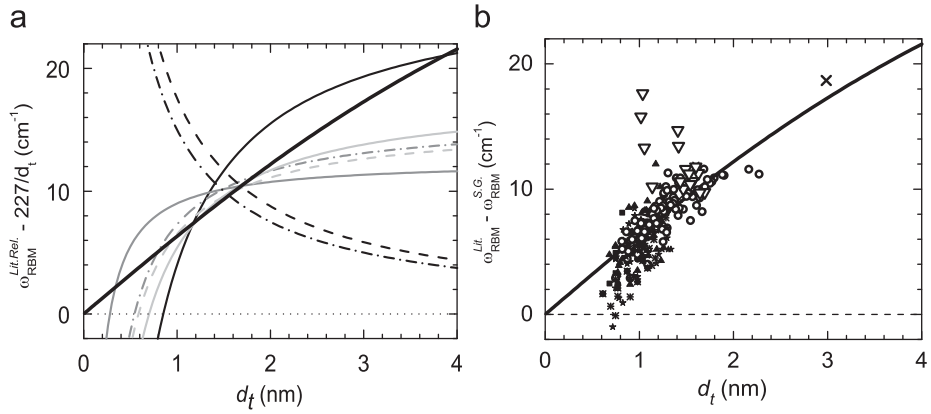

Fig. 2. (a) Difference between ω_{RBM} relations from the literature ($\omega_{RBM}^{Lit.Rel.}$) and $\omega_{RBM}=227.0/d_t$ as a function of tube diameter (d_t). Different line styles stand for different references, as listed in Ref. [13]. (b) Difference between ω_{RBM} data from the literature ($\omega_{RBM}^{Lit.}$) and ω_{RBM} data from the *S.G.* SWNTs ($\omega_{RBM}^{S.G.}$) as a function of d_t. Each symbol represents data from a different reference, as given in Ref. [13]. The thick solid line is a fit to the data in (b), as discussed in the text, and it is also shown in (a) [13].

[11,13–16,19,21,22] and the $\omega_{RBM}=227.0/d_t$ established for the *S.G.* sample. All the curves in the literature converge within the 1–2 nm d_t range, that is where most of the experimental data were actually obtained. Fig. 2(b) shows the difference between the ω_{RBM} experimental values from the literature ($\omega_{RBM}^{Lit.}$) [11,15–22] and from Ref. [13] ($\omega_{RBM}^{S.G.}$), as a function of d_t. All the published results for $\omega_{RBM}^{Lit.}$ are grouped in Fig. 2(b) on a d_t dependent trend for which $\Delta\omega_{RBM}=\omega_{RBM}^{Lit.}-\omega_{RBM}^{S.G.}$ is upshifted.

The $\Delta\omega_{RBM}$ upshift is explained by a molecular dynamics calculation considering van der Waals interactions between SWNTs and a shell of adsorbed fluid around the SWNT [49]. The van der Waals interactions occur between the SWNT π orbital and π or σ orbitals of the environment system [50]. Longhurst and Quirke [49] proposed a model that fits their molecular dynamics calculations, considering the RBM of a coupled system SWNT/environment composed of two spring constants: one coming from the C–C bond strength and the other coming from the interaction strength between the SWNT and its surroundings. The problem of addressing the environmental effect on ω_{RBM} is now reduced to solve a simple harmonic oscillator for a cylindrical shell subjected to an inwards pressure ($p(x)$) given by

$$\frac{2x(t)}{d_t^2}+\frac{\rho}{E}(1-\nu^2)\frac{\partial^2 x(t)}{\partial t^2}=-\frac{(1-\nu^2)}{Eh}p(x), \tag{1}$$

where $x(t)$ is the displacement in the radial direction, $p(x)=(24K/s_0^2)x(t)$, K (in eV/Å^2) gives the van der Waals interaction strength, s_0 is the equilibrium separation between the SWNT wall and the environment shell, E is Young's modulus, ρ is the mass density per unit volume, ν is Poisson's ratio and h represents the thickness of the shell. If $p(x)$ is null, Eq. (1) gives the fundamental ω_{RBM}^0 for a pristine SWNT

$$\omega_{RBM}^0=\left\{\frac{1}{\pi c}\left[\frac{Eh}{\rho h(1-\nu^2)}\right]^{1/2}\right\}\frac{1}{d_t}, \tag{2}$$

where the term inside the curly bracket is established here as 227.0 cm^{-1} nm, in agreement with the theoretical results using parameters from graphite [48]. Solving Eq. (1) for a non-null $p(x)$, one obtain

$$\omega_{RBM}=\frac{227}{d_t}\sqrt{1+C_e\cdot d_t^2}, \tag{3}$$

where $C_e=[6(1-\nu^2)/Eh][K/s_0^2]\,\mathrm{nm}^{-2}$.

The difference $\Delta\omega_{RBM}$ between the pristine relation $\omega_{RBM}=227/d_t$ and Eq. (3) is given by

$$\Delta\omega_{RBM}=\omega_{RBM}-\omega_{RBM}^0=227/d_t[\sqrt{1+C_e\cdot d_t^2}-1]. \tag{4}$$

This equation fits the results in Fig. 2(b) considering C_e=0.057 nm^{-2}, as shown by the black-solid curve.

3. The effect of the environment on the $\omega_{RBM}^{S.G.}$

The result discussed above gave rise to two different scenarios: one for the "super-growth" $\omega_{RBM}^{S.G.}=227/d_t$ and another for all the other RBMs reported in the literature, which were shown to be fitted by $\omega_{RBM}=(227/d_t)\sqrt{1+(0.057)\cdot d_t^2}$. For this reason, resonance Raman spectroscopy was used to study the ω_{RBM} of the "super-growth" SWNTs under three different conditions: (I) an as-grown carpet-like sample, (II) in solution, dispersed with a surfactant and (III) in bundles [51]. To quantify the changes in the RBM frequencies due to a change in the environment, Fig. 3 shows the spectrum for the "super-growth" SWNTs in a sodium dodecyl sulfate SDS solution (top), the Raman spectrum obtained for the bundled sample (middle) and the Raman spectrum for the as-grown "super-growth" SWNTs (bottom). In each spectrum, the raw spectra are fitted by Lorentzians representing the RBM features from SWNTs that are in resonance with the excitation laser and contribute to the spectra.

The arrows in Fig. 3 serve as a guide to the eyes, whereby we can easily realize that the frequencies for the solution and bundled samples, which from now on are called, respectively, $\omega_{RBM}^{solut.}$ and $\omega_{RBM}^{bundl.}$, are upshifted with respect to the as-grown values $\omega_{RBM}^{S.G.}$. In agreement with what is reported in Ref. [18], the larger the d_t value, the greater is the frequency upshift. No difference is observed between the $\omega_{RBM}^{solut.}$ and the $\omega_{RBM}^{bundl.}$, which suggests that the interactions between the tubes with their respective environments are in the same range of strength. Its worth to comment that the surfactant dramatically suppresses the Raman response of tubes with diameters higher than 0.9 nm ($d_t\leqslant 0.9$ nm) when in solution. When drying the bundled sample, the RBM response for tubes with diameters ranging from 0.9 to 1.3 nm is recovered. This result is consistent with experiments of absorption, photoluminescence and Raman scattering in other SWNTs samples [27–32].

Fig. 4 shows the differences between $\omega_{RBM}^{solut./bundl.}$ and $\omega_{RBM}^{S.G.}$ plotted as a function of d_t. The open circles stand for $\Delta\omega_{RBM}^{bundl.}=\omega_{RBM}^{bundl.}-\omega_{RBM}^{S.G.}$ and the down triangles stand for $\Delta\omega_{RBM}^{solut.}=\omega_{RBM}^{solut.}-\omega_{RBM}^{S.G.}$. The black solid line in Fig. 4, which fits the symbols, is given by Eq. (4) with C_e=0.056. This result shows that the ω_{RBM} for both solution and bundles are upshifted in relation to the frequencies observed in the as-grown sample, following exactly the same van der Waals interaction model that

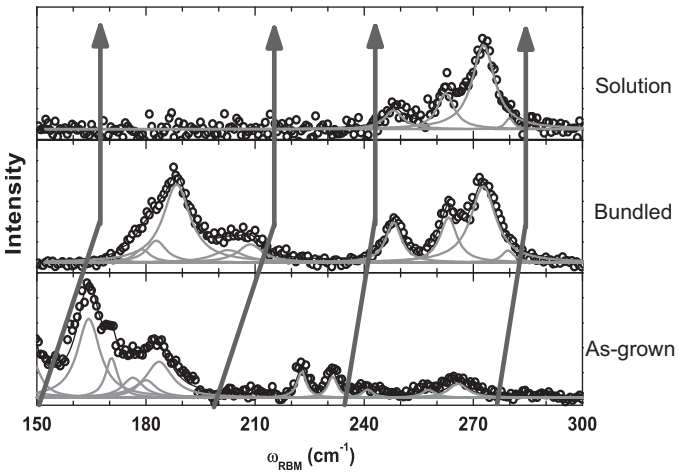

Fig. 3. The Raman spectrum obtained for: (top) the solution of "super-growth" SWNTs in SDS (middle) the bundled "super-growth" sample and (bottom) the as-grown sample. All the spectra were obtained by using $E_{laser} = 2.41$ eV (514.5 nm) and normalized to the highest intensity peak. The open circles represent the raw data and the solid gray curves are Lorentizians representing the RBMs from the SWNT species in resonance. The black solid line is the result obtained from the Lorentizian fitting procedure. The arrows are a guide to the eyes showing that the ω_{RBM} is upshifted for the solution and bundled samples, in comparison with the as-grown sample [51].

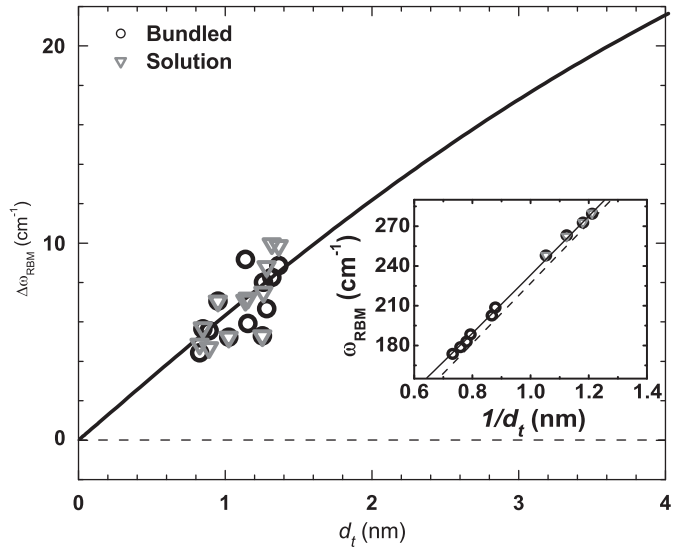

Fig. 4. The as-grown super-growth frequencies ($\omega^{S.G.}_{RBM}$) are subtracted from the frequencies of both solution (▽) and bundled (○) samples represented, respectively, by $\omega^{Solut.}_{RBM}$ and $\omega^{Bundl.}_{RBM}$, and plotted as a function of d_t. The solid curve describes the frequency shift behavior due to van der Waals interactions between the tube walls and their environment. Inset: $\omega^{solut./bundl.}_{RBM}$ plotted as a function of $1/d_t$, where the dashed line is given by $\omega^{S.G.}_{RBM} = 227/d_t$ and the solid line is given by $\omega^{solut./bundl.}_{RBM} = (227/d_t)\sqrt{1+0.056\cdot d_t^2}$ [51].

describes all the ω_{RBM} in the literature [13]. The two scenarios are now merged indicating that the as-grown "super-growth" SWNTs are, somehow, free from environmental effects.

4. The evolution of the experimental determination of E_{ii}

As briefly stated in the Introduction, quantum confinement is responsible for the occurrence of van-Hove singularities in the electronic structure of SWNTs, resulting in strong resonance processes. The last decade assembled much important experimental information about E_{ii} that, piece by piece, was supported by theoretical approaches by means of tight-binding and first-principles calculations [10,33–40,54]. In 2001, Jorio et al. [15] described E_{ii} by means of a first-neighbor tight-binding calculation combined with a zone-folding procedure. They successfully explained their experimental results using this simple model because the range of tube diameters ($1 < d_t < 3$ nm) and laser energy ($E_{laser} = 1.58$ eV) covered a region where curvature and excitonic effects were not evident [15]. In 2002, Bachilo et al. [16] performed Raman scattering and photoluminescence experiments on high-pressure carbon monoxide (HiPco) grown SWNTs dispersed in SDS and, by analyzing the experimental E^S_{11} and E^S_{22} values for semiconducting SWNTs, they figured out that the simple first-neighbor tight-binding calculation was not able to accurately describe the experimental E^S_{11} and E^S_{22} transition energies for SWNTs within the ($0.7 < d_t < 1.3$ nm) range.

For this reason, the so-called "ratio-problem" and the curvature effect were introduced, providing evidence that excitons and the $\sigma-\pi$ hybridization should be take into account. Popov et al. [36,37] and Samsonidze et al. [38] described the curvature effects by including many neighbors and a mixing of σ and π orbitals ($\sigma-\pi$ hybridization) in their tight-binding calculations, and these extensions became known as the extended tight-binding (ETB) model, while Spataru et al. [39], performing first-principle calculations, described the exciton structure directly. The ETB model was efficient in describing all ($2n+m$)-family trends, as reported by Telg et al. [19] and Fantini et al. [21]. Telg et al. and Fantini et al. used resonance Raman spectroscopy with a set of tunable lasers to map the RBM signal from HiPco SWNTs dispersed in SDS, building a 3D plot (see Fig. 5) from which they experimentally assigned more than 45 SWNTs, including S-SWNTs and M-SWNTs. Later, Wang et al. [52] and Maultzsch et al. [53] performed two-photons experiments giving rise to strong experimental evidence that the electronic transitions in SWNTs arise from excitons.

In 2007, the RBM spectra of as-grown vertically aligned SWNTs synthesized by the chemical vapor deposition method from alcohol were measured over a broad diameter (0.7–2.3 nm) and energy (1.26–2.71 eV) ranges [11]. Over 200 different SWNT species and about 380 different optical transition energies were probed, going up to the fourth optical transition of semiconducting SWNTs, thus establishing the (n, m) dependence of the poorly studied E^S_{33} and E^S_{44} transitions [11]. Over 95 different laser lines were used to generate the 2D plot giving the Raman intensity as a function of the laser excitation energy (E_{laser}) and the inverse of Raman frequency shift, as showed in Fig. 6. As stated in Section 2, the d_t is known to be related to the inverse ω_{RBM}, so that the resonance profile of each RBM Raman peak can be directly related to a given SWNT diameter.

Using the 2D plot exhibited in Fig. 6, 84 different SWNTs species were unambiguously indexed, allowing a careful analysis of E_{ii} to be made from E^S_{22} to E^S_{44}. For a fixed SWNT chirality, the E_{ii} values are expected to exhibit a simple scaling behavior when plotted as a function of p/d_t, where p=1, 2, 3, 4, 5 for E^S_{11}, E^S_{22}, E^M_{11}, E^S_{33}, E^S_{44}, respectively [40]. To a first approximation, considering the linear dispersion of the graphene close to the high-symmetry K-point and wavevector quantization along the circumference of the SWNT, the optical transition energies in carbon nanotubes are given by $E_{ii} = \hbar v_F(4p/3d_t)$ [10], where v_F is the Fermi velocity. The tube is metallic if p is a multiple of 3, and semiconducting otherwise [10]. For a fixed diameter, the E_{ii} values are expected to exhibit a comparably smaller dependence on the chiral angle θ (ranging from 0 to 30°) [10]. The chirality correction is null for armchair tubes ($\theta = 30°$) and is a maximum for zigzag tubes ($\theta = 0$), given approximately by $\beta_p \cos 3\theta/d_t^2$ [11].

Fig. 7(a) shows a plot of the assigned transition energies E^S_{11}, E^S_{22}, E^M_{11}, E^S_{33}, E^S_{44} as a function of p/d_t, after correction for their

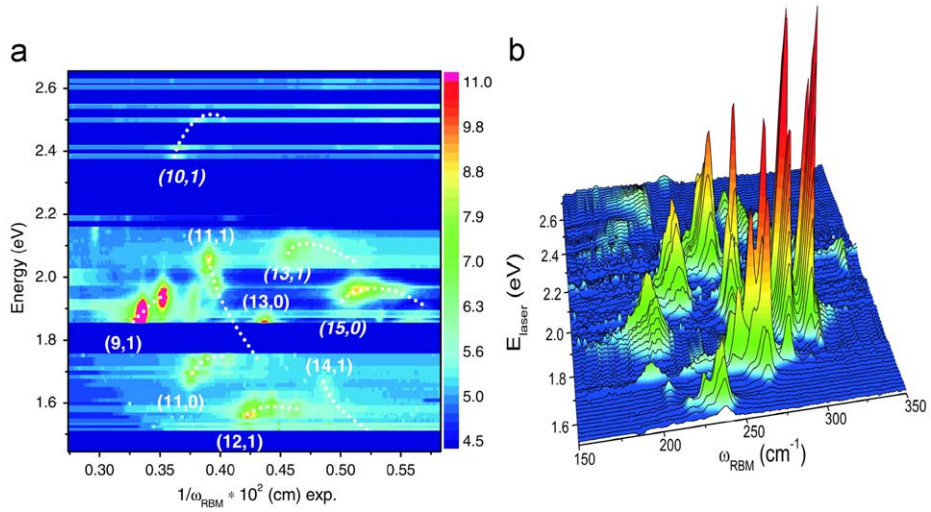

Fig. 5. (color online) (a) Contour plot of the Raman intensity of the RBM from HiPco SWNTs dispersed in a SDS aqueous solution as a function of excitation energy and reciprocal RBM frequency. The dotted and dashed lines connect maxima originating from tubes of the same $(2n+m)$=const. branch. In each branch the member with the smallest chiral angle ($\theta \to 0$) is labeled [19]. (b) RBM Raman measurements of a similar sample, measured with 76 different laser lines E_{laser} and showing results consistent with (a) [21].

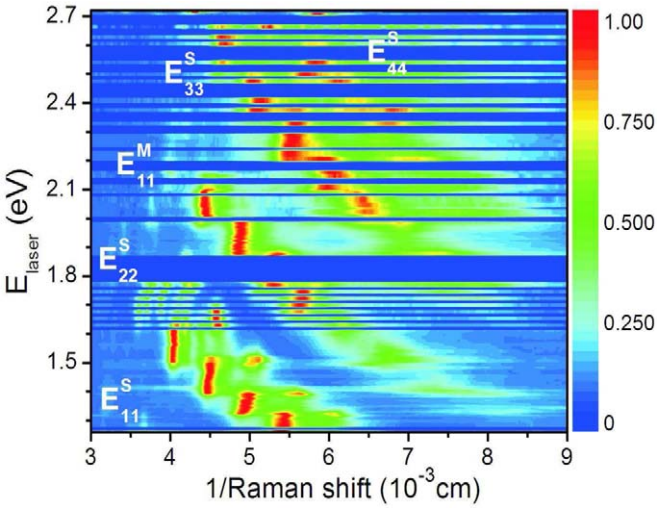

Fig. 6. (color online) 95 different laser lines were used to generate a 2D color map showing the RBM spectral evolution as a function of excitation laser energy for SWNTs growth by the alcohol assisted CVD method. The intensity of each spectrum is normalized to the strongest peak, and we plot the inverse Raman shift. The E_{ii} subbands are labeled with S/M superscripts standing for semiconducting/metal tubes [11].

chirality dependence obtained by subtracting ($\beta_p \cos 3\theta/d_t^2$) from the experimentally obtained E_{ii} values (see inset to Fig. 7(a) and respective caption for β_p values, $1 \le p \le 5$). Such a chirality correction is expected to collapse all E_{ii} values onto a single (p/d_t) dependent curve [40]. Note that the points do not scale linearly as p/d_t. As discussed by Kane and Mele [40], the non-linear scaling is due to many-body effects and can be fit with a logarithmic correction (see Eq. (5) further in the text). Its interesting to note is that the E^S_{33} and E^S_{44} transitions clearly do not follow the same scaling law as the E^S_{11} and E^S_{22} transitions, indicating that there is something fundamentally different between the first two lowest energy optical transitions and the subsequent transitions in semiconducting SWNTs. Fig. 7(b) shows evidence for the difference between the (E^S_{33}, E^S_{44}) and (E^S_{11}, E^S_{22}, E^M_{11}) experimental data. The E^S_{11}, E^S_{22} and E^M_{11} values plotted in Fig. 7(a) can be fitted by [40]

$$E_{ii}(p,d_t) = a\frac{p}{d_t}\left[1 + b\log\frac{c}{p/d_t}\right] + \beta_p \cos 3\theta/d_t^2, \quad (5)$$

with $a = 1.049\,\text{eV nm}$, b=0.456 and $c = 0.812\,\text{nm}^{-1}$. This functional form carries both the linear dependence of E_{ii} on p/d_t, expected from the quantum confinement of the 2D electronic structure of graphene, and the many-body logarithmic corrections [40]. Fig. 7(b) shows the deviation (ΔE) of the chirality dependence corrected ($E_{ii} - \beta_p \cos 3\theta/d_t^2$) values from the right side of Eq. (5). The deviations ΔE^S_{33} and ΔE^S_{44} from the zero line in Fig. 7(b) shows a clear $1/d_t$ dependence, and can be successfully fit by a single expression $\Delta E = \gamma/d_t$, with $\gamma = (0.305 \pm 0.004)\,\text{eV nm}$. Michel et al. [12] observed the same odd behavior finding also a $1/d_t$ dependent deviation.

Quantum-chemistry calculations were used to explain the scaling-law breakdown showing that the excitons related to higher transitions (E^S_{33}, E^S_{44},) are weakly bound (or are even unbounded e–h pairs) [11] due to the mixing of the DOS of E^S_{11} and E^S_{22} with E^S_{33}. At the bottom of the E^S_{33} zone there is a large DOS from E^S_{11} and E^S_{22}, corresponding to delocalized and unbound states. This effect is enhanced at the E^S_{33} and E^S_{44} levels compared to the E^S_{22} states (the latter overlaps only with the E^S_{11} band). The calculations estimate less than 0.001 eV separation in the density of states at the E^S_{33} transition, attributed to other molecular states, compared to about a 0.02 eV separation at the E^S_{22} transition. Any small perturbation (e.g. dielectric environment inhomogeneity, tube ends or vibrational coupling) will strongly mix the nearly isoenergetic states at the E^S_{33} and E^S_{44} levels. Consequently the mixing of all these states and non-Condon effects might become important with E^S_{33} and E^S_{44} only marginally reflecting the character of "pure" states [11].

However, predictions based on solid-state physics calculations, both tight binding and first-principles, actually give an opposite picture, i.e. that the excitons which are related to the higher transitions are more strongly bounded than the lower ones, and the stronger many-body effects cause the breakdown of the scaling law [34,35]. A reason why higher transitions exciton states are strongly bounded is that the effective mass of electron and hole in these higher transitions are heavier than in the lower transitions [34]. Thus the corresponding Coulomb energy (electron self-energy and exciton biding energy) increases as a

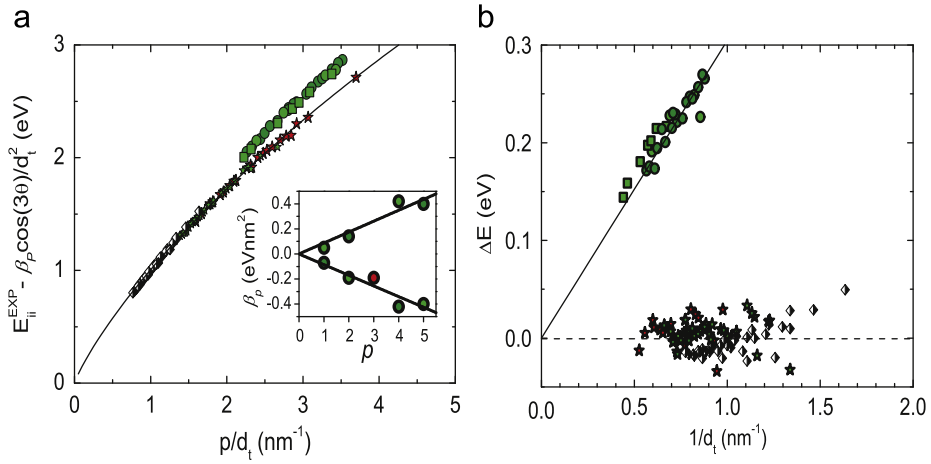

Fig. 7. (color online) (a) Experimental optical transition energies as a function of p/d_t, after correcting for the chiral angle dependence ($E_{ii}^{EXP} - \beta_p \cos 3\theta/d_t^2$). The chirality dependence corrected E_{11}^S (black and white diamonds from Ref. [16]), E_{22}^S (green/olive stars) and E_{11}^M (red stars) are fitted with Eq. (5). Inset: the experimental β_p values for the lower (upper) E_{ii} branches are −0.07(0.05), −0.19(0.14), −0.19 (not measured), −0.42(0.42) and −0.4(0.4) for p=1, 2, 3, 4 and 5, respectively. (b) Deviation (ΔE) of the ($E_{ii}^{EXP} - \beta_p \cos 3\theta/d_t^2$) data from the fitting curve in (a), versus $1/d_t$. The solid line ($\Delta E = 0.305/d_t$) fits the ΔE_{33}^S (green/olive circles) and ΔE_{44}^S (squares) [11].

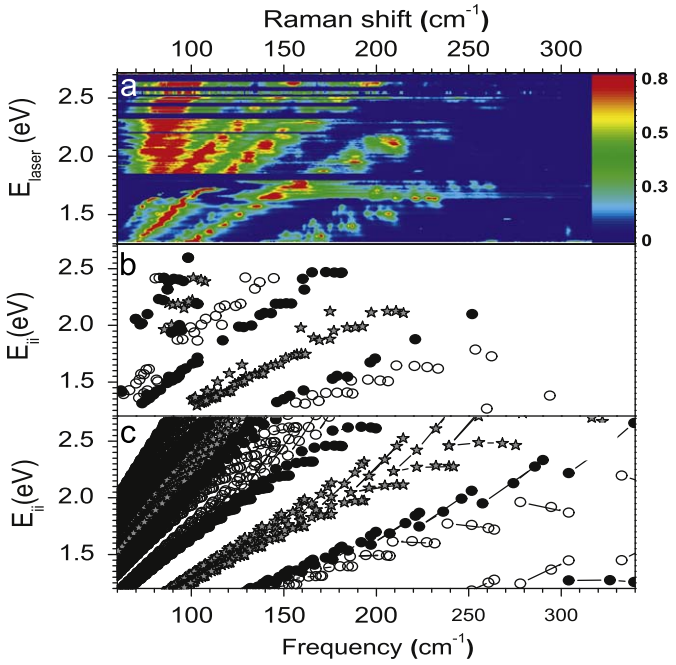

Fig. 8. (color online) (a) 2D color map showing the "super-growth" SWNT RBM spectral evolution as a function of laser excitation energy. The intensity of each spectrum is normalized to the strongest peak. (b) Plot of all transitions energies (E_{ii}) experimentally obtained as a function of ω_{RBM}. (c) The Kataura plot for "super-growth" SWNTs. The transition energies were calculated using Eq. (5), that is obtained by fitting the available E_{ii} (panel (b)) and plotted as a function of ω_{RBM}, given by $\omega_{RBM} = 227/d_t$ (see Section 2). In (b) and (c) the gray stars stand for metallic tubes, the black bullets stand for type I semiconducting tubes and the opened bullets stand for type II semiconducting tubes. Type I and II are defined by $(2n+m) \bmod 3 = 1, 2$, respectively [55].

function of the exciton wavevector measured from the high symmetry K-point in the 2D brillouin zone. Therefore, the opposite conclusions come from opposite pictures given by different theoretical models. While solid state physics based calculations impose periodic boundary conditions on a perfect tube and the exciton wavevector constitutes a good quantum number, which allows efficient separation of "pure" E_{11}^S, E_{22}^S, and E_{33}^S bands, quantum-chemistry calculations do not impose periodic boundary conditions and do not allow such separation. On the other hand, quantum chemistry calculations are based on a short SWNT segments (about 500 atoms in Ref. [11]). The experimental results themselves did not offer a conclusive answer towards one or the other theoretical model, which led us to a deep search for the missing physics; i.e. the dielectric screening discussed in Section 5.

In 2008, similar resonance Raman experiments were performed in the "super-growth" SWNTs. The scaling law breakdown mentioned above was confirmed [55,56]. Using over 125 different laser lines, 197 SWNTs were properly assigned with transition energies ranging from E_{11}^S to E_{66}^S (see Fig. 8). By doing a similar E_{ii} analysis as performed for the "alcohol-assisted" CVD SWNTs, the new parameters for Eq. (5), which fit the experimental data for the *S.G.* SWNTs are: $a = 1.074$ eV nm, b=0.467 and c=0.812 nm^{-1}. For transition energies higher than E_{11}^M, the p/d_t dependent term $0.059p/d_t$ has to be added. The β_p values for the lower (upper) E_{ii} branches are −0.07(0.09), −0.18(0.14), −0.19(0.29), −0.33(0.49), −0.43(0.59), −0.6(0.57), −0.6(0.73) and −0.65 (not measured) for $p = 1, 2, 3, \ldots, 8$, respectively. A comparative analysis with data available in the literature revealed that all the E_{ii} for the "super-growth" SWNTs were upshifted by ∼40 meV in average, relative to all the other values reported in the literature, although this upshift is d_t dependent [55].

Interestingly, while the higher energy branch of the E_{11}^M values was not observed for the measurements shown in Figs. 5 and 6, the *S.G.* sample gave a set of data for both the higher and lower energy E_{11}^M for metallic nanotubes [56]. When the scaling law analysis is applied to the metallic E_{ii}, the data for both upper and lower branches closely match the semiconducting trendlines [56], i.e. E_{11}^M follows (E_{11}^S, E_{22}^S), while E_{22}^M follows (E_{33}^S, E_{44}^S). The excellent representation of the trend in the metallic transition energies by the semiconductor logarithmic scaling law is indirect evidence that the metallic transitions are also excitonic in nature. If one first assumes no exciton, then it is possible that significant metallic screening reduces the E_{11}^M self-energies sufficiently to allow for a coincidental overlap with the E_{11}^S and E_{22}^S scaling line. A simultaneous overlap of E_{22}^M with the E_{33}^S and E_{44}^S scaling line, however, is unlikely in the absence of the exciton. Lack of a binding-energy stabilization for E_{22}^M would cause its scaling line to appear above the E_{33}^S and E_{44}^S line, which is not the case. Thus, the existence of excitons in these 1D metals is strongly suggested over the full diameter and energy ranges measured [56].

5. The role of dielectric screening on E_{ii}

The assignments of E_{ii} for SWNTs over a large region of both d_t (0.7–3.8 nm) and E_{ii} (1.2–2.7 eV) values and for a variety of surrounding materials are now available [11–32], thus making it possible to accurately determine the effect of changing environment in E_{ii}. The calculated E_{ii} values can be renormalized by explicitly considering the dielectric constant κ in the Coulomb potential energy $V(q)/\varepsilon(q)\kappa$ [41]. Here, κ represents the screening of the e–h (electron–hole) pair by core (1s) and σ electrons (κ_{tube}) and by the surrounding materials (κ_{env}). $\varepsilon(q)$ explicitly gives the polarization function for π- electrons calculated within the random phase approximation (RPA) [14,35,57,58]. Fig. 9 shows a map of the "super-growth" experimental E_{ii} values ($E_{ii}^{\text{exp.}}$) (black dots) plotted as a function of their ω_{RBM}. The "super-growth" sample was chosen for the initial analysis because the sample has a homogeneous environment and a large variety of SWNT diameters, as measured by RRS. Furthermore, this sample shows the fundamental relation $\omega_{\text{RBM}} = 227/d_t$ [13] and the highest E_{ii} values in the literature [55]. This last result indicates that the tubes are surrounded by the lowest environmental dielectric constant ($\kappa_{\text{env}} \to 1$) reported in the literature. Furthermore, the previously elusive high energy branches for the transitions for metallic tubes are observed, indicating the lowest degree of perturbation to this sample. The $E_{ii}^{\text{exp.}}$ are compared with the calculated bright exciton energies E_{ii}^{cal} (open circles and stars). Although E_{ii}^{cal} includes SWNT curvature and many-body effects [35], the $E_{ii}^{\text{exp.}}$ values are clearly red shifted when compared with theory, and the red shift depends on ω_{RBM}, i.e. on d_t, and on the optical levels (i in E_{ii}). To fully account for the observed energy-dependent E_{ii} red shift, we must fit the total κ values ($1/\kappa = C_{\text{env}}/\kappa_{\text{env}} + C_{\text{tube}}/\kappa_{\text{tube}}$) to minimize $E_{ii}^{\text{exp}} - E_{ii}^{\text{cal}}$ and the results will be discussed in connection with Fig. 11.

However, to gain more insights about the influence of κ on E_{ii}, the "alcohol-assisted" SWNTs [11] were chosen for a comparative analysis with the "super-growth" SWNTs. This comparative analysis led us to a semi-empirical understanding of the role of the dielectric constant in E_{ii}. Fig. 10 shows the experimental Kataura's plot for these two samples, where both E_{ii} and ω_{RBM} change from one sample to another. The "alcohol-assisted" SWNTs were chosen for comparison because: (1) this sample also has a broad diameter distribution ($0.7 < d_t < 2.3$ nm); (2) the observed E_{ii} are similar to many other samples in the literature [11,13,55]; (3) the sample is morphologically similar to the "super-growth" sample (both are carpet-like free standing SWNTs). Looking at Fig. 10, the E_{ii} values for the "alcohol-assisted" SWNTs are all downshifted with relation to the E_{ii} values for the "super-growth" SWNTs. Since the κ_{tube} does not change for any SWNT, the $\kappa_{\text{env.}}$ must be higher for the "alcohol-assisted" tubes.

Fig. 11 show the fitted κ values as a function of p/d_t, which reproduce each experimental E_{ii} value for the assigned (n, m) SWNTs for the "super-growth" SWNT sample (bullets). The stars stand for the "alcohol-assisted" SWNTs. For E_{22}^S and E_{11}^M (Fig. 11(a)), up to $p=3$, we see a clear difference for κ. However, for E_{33}^S and E_{44}^S (Fig. 11(b)), no difference in κ can be seen between these two types of sample. This means that the electric field of the E_{33}^S and E_{44}^S excitons do not extend much outside the SWNT volume, in contrast to the E_{22}^S and E_{11}^M excitons for which the κ_{env} effect is significant. Since the effect of κ_{env} is relatively small for energies above E_{11}^M, it is possible to assign the (n, m) values from E_{33}^S and E_{44}^S even if the dielectric constant of the environment is not known, even though the E_{33}^S and E_{44}^S values are seen within a large density of dots in the Kataura plot. The data in Fig. 11 were fitted with the relation

$$\kappa = C_\kappa \left(\frac{p}{d_t}\right)^{1.7}, \tag{6}$$

where the exponent 1.7 was found to work for all E_{ii}^{exp}, but different C_κ parameters are needed for different samples. For E_{11}^S, E_{22}^S and E_{11}^M, $C_\kappa = 0.75$ for the "super-growth" SWNTs and $C_\kappa = 1.02$ for the "alcohol-assisted" SWNTs (dashed and dotted curves in Fig. 11(a), respectively). The E_{33}^S and E_{44}^S are fitted using $C_\kappa = 0.49$ for both samples, as shown by the dashed line in Fig. 11(b). As reported in Ref. [41], by renormalizing the calculated E_{ii} using Eq. (6) with the C_κ parameters given above, all the experimental E_{ii} for both the "super-growth" and the "water-assisted" SWNT samples can be understood within an accuracy of 70 meV.

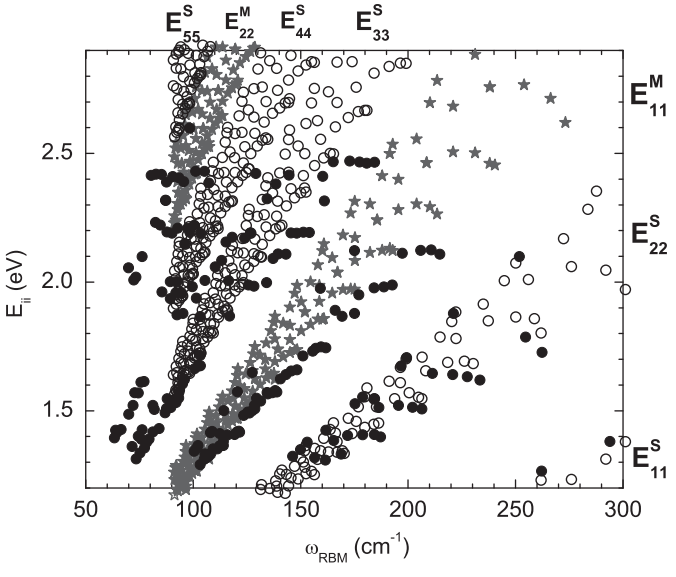

Fig. 9. Black dots show E_{ii}^{exp} vs. ω_{RBM} results obtained from resonance Raman spectra taken from the "super-growth" SWNT sample [13,55]. The black open circles (semiconducting) and the dark-gray stars (metallic) give E_{ii}^{cal} for the bright exciton calculation with dielectric constant $\kappa = 1$ [35]. Along the x-axis, E_{ii}^{cal} are translated using the relation $\omega_{\text{RBM}} = 227/d_t$ [13]. Due to the long computer time needed for this calculations, only E_{ii} for tubes with $d_t < 2.5$ nm (i.e. $\omega_{\text{RBM}} > 91\,\text{cm}^{-1}$) have been calculated. Transition energies E_{ii}^S ($i = 1-5$) stand for semiconducting and E_{ii}^M ($i = 1, 2$) stand for metallic SWNTs [41].

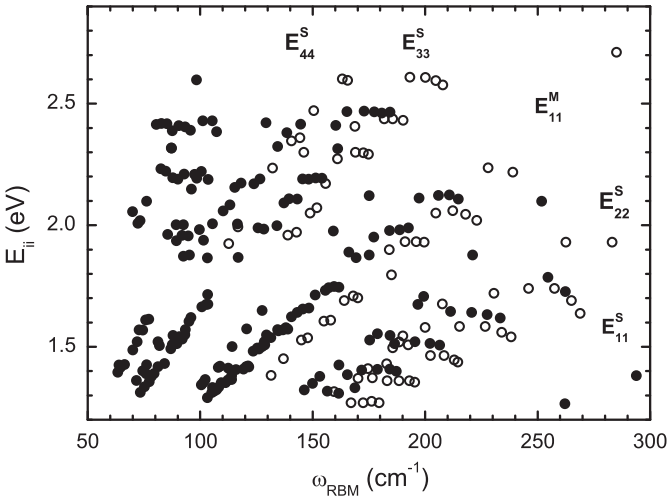

Fig. 10. E_{ii}^{exp} vs. ω_{RBM} results obtained for the "super-growth" (filled circles) and "alcohol assisted" (open circles) SWNT samples [41].

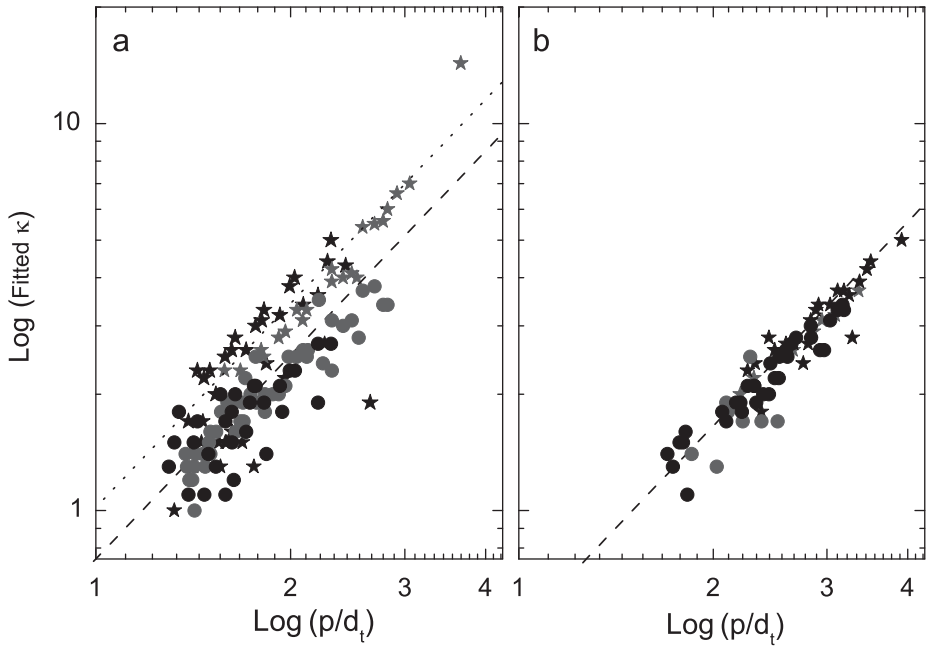

Fig. 11. The calculated κ, which are fitted to the experimental E_{ii} values from the "super-growth" (bullets) [55] and "alcohol-assisted" (stars) [11] samples. (a) E^S_{22} (black) and E^M_{11} (dark-gray). The dashed and dotted curves are given by Eq. (6) with $C_\kappa = 0.75$ and 1.02, respectively. (b) E^S_{33} (black) and E^S_{44} (dark-gray). The dashed curve is for Eq. (6) with $C_\kappa = 0.49$ [41].

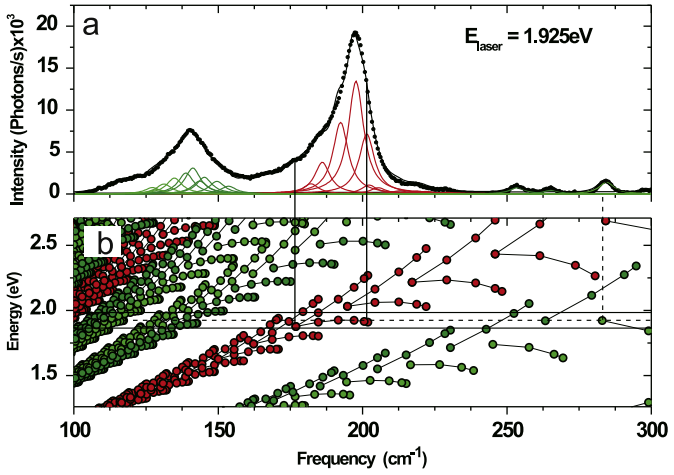

Fig. 12. (a) Raman spectrum (bullets) obtained with a 644 nm laser line (1.925 eV). This spectrum was fitted by using 34 Lorentizians (curves under the spectra) and the solid line is the fitting result. (b) The Kataura plot from Eq. (5). The dashed line indicates E_{laser} and the solid line gives the width of the resonance window ($E_{\text{laser}} \pm 0.06$) eV [11].

6. A guide for the (n, m) assignment

The Raman-based (n, m) assignment is straightforward if the sample has isolated tubes or even bundles with small diameter tubes. In this case, the RBM spectra have well defined ω_{RBM} peaks (Fig. 5). The (n, m) assignment becomes more difficult when the sample is composed of SWNTs with a broad range of d_t (Fig. 8). The larger the d_t, the larger the overlap in the resonances among different RBMs for tubes of similar d_t. In this case, the assignment must be performed based on anchors, as discussed further in the text.

Let us begin with just one laser line. Fig. 12(a) shows one RBM spectrum obtained using the 644 nm laser line ($E_{\text{laser}} = 1.925$ eV). Fig. 12(b) shows the Kataura plot used to analyze the spectra, obtained from Eq. (5) using the parameters for the "alcohol-assisted" CVD grown SWNTs. Each bullet represents one transition energy ($E^{M,\ S}_{ii}$). From the bottom to the top, the first group is associated with the E^S_{22} (E^S_{11} is below and only a single point can be seen at the right-bottom corner), the second group is the E^M_{11}, the third group is the E^S_{33}, and so on. The light green bullets are associated with semiconductor carbon nanotubes with $\text{mod}(2n+m, 3) = 1$ (type one—SI), the olive bullets are associated with semiconductor carbon nanotubes with $\text{mod}(2n+m, 3) = 2$ (type two—SII) and the red bullets are associated with metallic carbon nanotubes ($\text{mod}(2n+m, 3) = 0$). In each group, we can realize several branches, called families, that are characterized by $2n+m = \text{const}$. The geometrical patterns are crucial for the fitting (mainly in case one has a map with many laser lines), and they work for larger diameter tubes as well.

In Fig. 12(a) the bullets show the data and the solid line shows the fit obtained using 34 Lorentzian curves (the peaks below the spectral curve). Each Lorentzian curve can be related to one RBM from one carbon nanotube. The red Lorentzians represent the RBM from metallic tubes and the green (olive) Lorentzians represent the RBM from semiconducting SI (SII) tubes. To know how many Lorentzians should be used to fit each resonance spectrum, we use the Kataura plot. Fig. 12(b) has a dashed line that represents the excitation energy for the spectrum shown in Fig. 12(a), and the two bold lines (above and below the dashed line) give the approximate boundary for the RBM resonance profiles (see the detailed discussion about the resonance profile in the next section). To fit the spectrum shown in Fig. 12(a) we expect that all the circles inside the rectangle ($E_{\text{laser}} \pm 0.06$) eV made by the two bold lines should show up. The vertical bold lines connecting Figs. 12(a) and (b) indicate the metallic $2n+m=30$ family in resonance. Note that while the Kataura plot usually presents E_{ii} as a function of d_t, in Fig. 12(b), we plot E_{ii} as a function of ω_{RBM} for a direct comparison with each spectrum. Here we have the first constraint:

- The conversion between ω_{RBM} and d_t must be performed considering the relation $\omega_{\text{RBM}} = (227/d_t)\sqrt{1 + C_e \cdot d_t^2}$. By properly adjusting the constant C_e one can overlap the bullets in

Kataura's plot within ($E_{laser} \pm 0.06$) eV and RBM peaks in the spectrum.

The difficulty in performing the spectral fitting occurs because a large number of Lorentzian curves are needed to fit a broad RBM profile. The fitting program tends to broaden and increase some peaks, while eliminating others. If for the same fit, one Lorentzian is shifted by a couple of cm^{-1}, the fitting program will return a completely different fitting result. Therefore, another constraint, this time for the linewidths (full width at half maximum—FWHM), must be adopted:

- We require all the Lorentzian peaks in one spectrum to share the same FWHM. The value is free to vary as a fitting parameter, but it should be the same for all Lorentzian peaks. Fluctuations of the RBM FWHM with (n, m) can be expected. However, such fluctuations do not change the picture of the results obtained after a self-consistent, many-cycles, fitting procedure.

After the fitting, one is ready to associate each pair (E_{laser}, ω_{RBM}) with a specific (n, m). With just one laser line ($E_{laser} \pm 0.06$) eV, the assignment procedure is reliable enough to associate a given ω_{RBM} to a couple (n, m) if the E_{ii} values are well known. However, as we said in Section 4, a change in κ changes E_{ii} and adds uncertainty in energy. For those using just one laser line this uncertainty is accounted for considering that a change in the environment changes E_{ii} by ~ 40 meV in average (see Section 5), although this value can go up to 100 meV giving rise to a new freedom in the fitting. An additional anchor here, to decrease the uncertainty, is the fact that, as the chiral angle gets smaller ($\theta \to 0$), the Raman signal gets more intense, as discussed in Section 7. In fact, the uncertainty in E_{ii} is promptly overcome by using many laser lines, allowing measurement of resonance profiles of each SWNT. After analyzing all the spectra obtained experimentally using the procedure described above for one laser line, we select each RBM frequency and plot its intensity as a function of E_{laser}. Such a plot gives the resonance profile for the SWNT that has the specified RBM mode frequency. Fig. 13 shows three Raman spectra for three E_{laser} values that are different but close to each other, so that the same RBMs should be close to resonance for the three spectra. In each spectrum we selected two Lorentzian curves (with frequencies around 192 and 186 cm^{-1}) and we show, in Figs. 13(d) and (e), their resonance profiles (intensity vs. E_{laser}). These resonance profiles should then be fit by using the RRS intensity equation:

$$I(E_{laser}, E_{ph}) = \left| \frac{\mathcal{M}}{(E_{laser} - E_{ii} - i\gamma)(E_{laser} - E_{ii} - E_{ph} - i\gamma)} \right|^2, \quad (7)$$

where $\mathcal{M}$ represents the matrix elements, E_{laser} is the laser energy, E_{ii} is the optical transition energy, γ is the resonance window linewidth and E_{ph} is the RBM energy. We assume the matrix elements and γ do not change within one resonance profile. From the fits it is then possible to obtain the E_{ii} for that specific RBM, i.e. for that specific (n, m) SWNT.

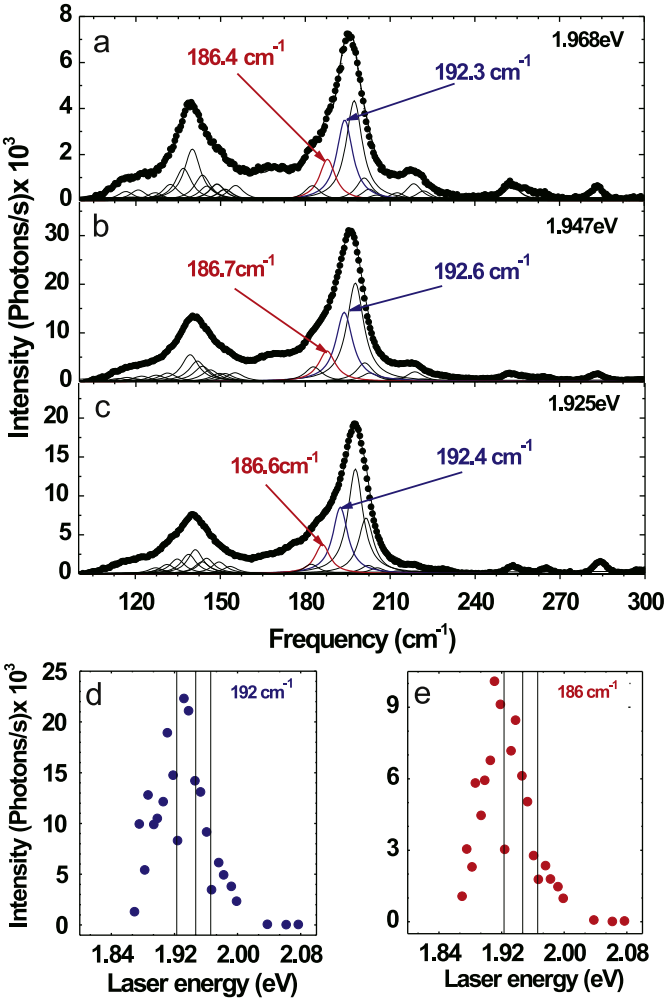

Fig. 13. Raman spectra (bullets) obtained with a (a) 630 nm (1.968 eV), (b) 637 nm (1.947 eV) and (c) 644 nm (1.925 eV) laser lines. All the spectra are fit with a sum of Lorentizians (solid line). (d) The resonance profile for the carbon nanotube with $\omega_{RBM} \sim 192$ cm^{-1}, (n, m)=(12,6). (e) The resonance profile for the carbon nanotube with $\omega_{RBM} \sim 186$ cm^{-1}, (n, m)=(11,8). The vertical lines indicate the three excitation energies used to measure the spectra displayed on panels (a), (b) and (c) [11].

7. The (n, m) dependence of the RBM intensity

Figs. 6 and 8 show the experimental RRS map where each spectrum was normalized to the strongest peak. Specially noticeable is the change in intensity within a given $(2n+m)$ = constant branch. The RBM signal gets stronger when going to smaller chiral angles ($\theta \to 0$). Since each spectrum ($S_{(\omega,E_L)}$) is the sum of the individual contributions of all SWNTs, it can be written as [59]

$$S_{(\omega,E_L)} = \sum_{n,m} \left[\mathrm{Pop}_{(n,m)} I(E_{laser}, E_{ph}) \frac{\Gamma/2}{(\omega - \omega_{RBM})^2 + (\Gamma/2)^2} \right], \quad (8)$$

where $\mathrm{Pop}_{(n,m)}$ is the population of the (n, m) nanotube species, $\Gamma = 3$ cm^{-1} is the experimental average value for the full width at half maximum intensity of the tube's RBM Lorentzian, ω_{RBM} is the frequency of its RBM and ω is the Raman shift.

Each nanotube in the sample contributes to the RBM RRS spectra with one Lorentzian, whose intensity ($I(E_{laser}, E_{ph})$) for the Stokes process at a given excitation laser energy (E_L) is given by Eq. (7). $\mathcal{M}$ represents the matrix elements for the Raman scattering by one RBM phonon of the (n, m) nanotube. The values

Table 2
Fitted parameters $\mathcal{M}_i$ and γ_i for metallic, semiconductor type I and type II tubes.

Type	$\mathcal{M}_A$	$\mathcal{M}_B$	$\mathcal{M}_C$	γ_A	γ_B	γ_C
M	1.68	0.52	5.54	23.03	48.84	1.03
S_1	−19.62	29.35	4.23	−3.45	65.10	7.22
S_2	−1.83	3.72	1.61	−10.12	42.56	−6.84

These parameters are to be used in Eqs. (9) and (10) with d_t in nm, yielding $\mathcal{M}$ in arbitrary units and γ in meV.

for E_{ii} and $E_{ph}=\hbar\omega_{\mathrm{RBM}}$ are determined experimentally, as stated earlier in the text. $\mathcal{M}$ and γ were found by fitting the experimental RBM RRS map in Fig. 8 with Eq. (8) using the functions:

$$\mathcal{M}=\left[\mathcal{M}_{\mathrm{A}}+\frac{\mathcal{M}_{\mathrm{B}}}{d_t}+\frac{\mathcal{M}_{\mathrm{C}}\cos(3\theta)}{d_t^2}\right]^2 \tag{9}$$

and

$$\gamma=\gamma_{\mathrm{A}}+\frac{\gamma_{\mathrm{B}}}{d_t}+\frac{\gamma_{\mathrm{C}}\cos(3\theta)}{d_t^2}, \tag{10}$$

where $\mathcal{M}_i$ and γ_i ($i=\mathrm{a},\mathrm{b},\mathrm{c}$) are adjustable parameters. The best values for $\mathcal{M}_i$ and γ_i, considering the excitonic transitions E_{22}^S and the lower branch of E_{11}^M are listed in Table 2 for d_t in nm, γ in meV and $\mathcal{M}$ in arbitrary units. Using these values in Eq. (8), we can model the map shown in Fig. 8, representing very well the experimentally observed results [59]. Thus is an important procedure for quantifying (n, m) dependent population, as described in Ref. [59].

8. Conclusions

Section 2 showed that a special class of SWNTs, called "super-growth", has their ω_{RBM} related to the d_t by the $\omega_{\mathrm{RBM}}=227/d_t$ relation. This relation is noticeable because it recovers the SWNT graphene sheet limit which says that $\omega_{\mathrm{RBM}}\longrightarrow 0$ when $d_t\longrightarrow\infty$. Furthermore, all the ω_{RBM} in the literature were found to be upshifted with relation to the "super-growth" $\omega_{\mathrm{RBM}}^{S.G.}$. This upshift was explained with basis on the van der Waals forces which mediate the interactions between the tube wall and the surrounding environment. In Section 3 it was shown that, by dispersing the "super-growth" tubes in sodium dodecyl sulfate (SDS) or bringing them into bundles, the "super-growth" ω_{RBM} is upshifted following the same behavior as the ω_{RBM} from the literature for other SWNT samples. Therefore, any measured $\omega_{\mathrm{RBM}}(d_t)$ for an arbitrary experimental sample are fitted to the formula $\omega_{\mathrm{RBM}}=(227/d_t)\sqrt{1+C_e\cdot d_t^2}$ where only a single parameter (C_e) is used to account for the observed d_t-dependent environmental effects. For the case of the "super-growth" SWNTs, we have a fit to the ω_{RBM} data for $C_e=0$, while for an arbitrary sample measured in the laboratory, a least squares fit is made by the researchers themselves to determine the best fit value for C_e.

Section 4 brought an overview of the RRS research on E_{ii} and gave a general equation for E_{ii} as a function of (d_t,θ), i.e for building Kataura's plot. Section 5 showed that the effective dielectric constant κ scales with d_t as: $\kappa=C_\kappa(p/d_t)^{1.7}$. For E_{11}^S, E_{22}^S and E_{11}^M, C_κ was found equals to 0.75 for the "super-growth" SWNTs and equals to 1.02 for the "alcohol-assisted" SWNTs. However, E_{33}^S and E_{44}^S are fitted using $C_\kappa=0.49$ for both samples, showing evidence that these higher transitions are not sensitive to a changing environment, while E_{11}^S, E_{22}^S and E_{11}^M are.

Section 6 gave a routine for performing (n, m) assignment of SWNTs in case one is using one or many laser lines. It was shown how the d_t scale in Kataura's plot must be converted into ω_{RBM} in order to directly compare to the experimental resonant Raman spectrum. Such conversion must be performed by using the relation $\omega_{\mathrm{RBM}}=(227/d_t)\sqrt{1+C_e\cdot d_t^2}$. Once this adjustment is done, one is ready to associate each pair $(E_{\mathrm{laser}},\omega_{\mathrm{RBM}})$ to a specific (n, m) if the E_{ii} values are well known. For those using one laser line, although the E_{ii} value cannot be precisely obtained, the assignment is reliable enough for correlating a given ω_{RBM} to its (n, m) index. Many laser lines are needed in case one wants to have reliable information about E_{ii}. Finally, Section 7 briefly discussed the (n, m) dependence of the RBM Raman intensity.

Acknowledgments

P.T.A., P.B.C.P and A.J. acknowledge financial support from FAPEMIG, Rede de pesquisa em nanotubos de carbono MCT/CNPq and AFORS/SOARD (award #FA9550-08-1-0236). M.S.D. acknowledges support from NSF Grant DMR07-04197. K.S. is supported by JSPS Research Fellowships for Young Scientists (No. 20-4594). R.S. acknowledges support from NEXT Grants (No. 20241023).

References

[1] C. Dekker, Phys. Today 52 (1999) 22.
[2] A. Javey, Nature 424 (2003) 654.
[3] P.L. McEuen, M.S. Fuhrer, H.K. Park, Nanotechnol. 1 (2002) 78.
[4] A. Bachtold, P. Hadley, T. Nakanishi, C. Dekker, Science 294 (2001) 1317.
[5] P.G. Collins, M.S. Arnold, P. Avouris, Science 292 (2001) 706.
[6] M. Endo, C. Kim, K. Nishimura, T. Fujino, K. Miyashita, Carbon 38 (2000) 183.
[7] E. Kimakis, G.A.J. Amaratunga, Appl. Phys. Lett. 80 (2002) 112.
[8] E. Kimakis, G.A.J. Amaratunga, Rev. Adv. Mater. Sci. 10 (2005) 300.
[9] M.S. Dresselhaus, G. Dresselhaus, R. Saito, A. Jorio, Phys. Rep. 409 (2005) 47.
[10] A. Jorio, M.S. Dresselhaus, G. Dresselhaus, Carbon Nanotubes: Advanced Topics in the Synthesis, Structure, Properties and Applications, Springer Series on Topics in Applied Physics, vol. 111, Springer, Berlin, 2008, p. 111.
[11] P.T. Araujo, S.K. Doorn, S. Kilina, S. Tretiak, E. Einarsson, S. Maruyama, H. Chacham, M.A. Pimenta, A. Jorio, Phys. Rev. Lett. 98 (2007) 067401.
[12] T. Michel, M. Paillet, J.C. Meyer, V.N. Popov, L. Henrard, J.-L. Sauvajol, Phys. Rev. B 75 (2007) 155432.
[13] P.T. Araujo, I.O. Maciel, P.B.C. Pesce, M.A. Pimenta, S.K. Doorn, H. Qian, A. Hartschuh, M. Steiner, L. Grigorian, K. Hata, A. Jorio, Phys. Rev. B 77 (2008) 241403(R).
[14] M. Milnera, J. Krti, M. Hulman, H. Kuzmany, Phys. Rev. Lett. 84 (2000) 1324.
[15] A. Jorio, R. Saito, J.H. Hafner, C.M. Lieber, M. Hunter, T. McClure, G. Dresselhaus, M.S. Dresselhaus, Phys. Rev. Lett. 86 (2001) 1118.
[16] S.M. Bachilo, M.S. Strano, C. Kittrell, R.H. Hauge, R.E. Smalley, R.B. Weisman, Science 298 (2002) 2361.
[17] A. Hartschuh, H.N. Pedrosa, L. Novotny, T.D. Krauss, Science 301 (2003) 1354.
[18] M. Strano, S.K. Doorn, E.H. Haroz, C. Kittrell, R.H. Hauge, R.E. Smalley, Nano Lett. 3 (2003) 1091.
[19] H. Telg, J. Maultzsch, S. Reich, F. Hennrich, C. Thomsen, Phys. Rev. Lett. 93 (2004) 177401.
[20] S.K. Doorn, D.A. Heller, P.W. Barone, M.L. Usrey, M.S. Strano, Appl. Phys. A 78 (2004) 1147.
[21] C. Fantini, A. Jorio, M. Souza, M.S. Strano, M.S. Dresselhaus, M.A. Pimenta, Phys. Rev. Lett. 93 (2004) 147406.
[22] M. Paillet, T. Michel, J.C. Meyer, V.N. Popov, L. Henrard, S. Roth, J.L. Sauvajol, Phys. Rev. Lett. 96 (2006) 257401.
[23] J. Lefebvre, J.M. Fraser, Y. Homma, P. Finnie, Appl. Phys. A 78 (2004) 1107.
[24] Y. Ohno, S. Iwasaki, Y. Murakami, S. Kishimoto, S. Maruyama, T. Mizutani, Phys. Rev. B 73 (2006) 235427.
[25] H. Son, A. Reina, Ge.G. Samsonidze, R. Saito, A. Jorio, M.S. Dresselhaus, J. Kong, Phys. Rev. B 74 (2006) 073406.
[26] M.Y. Sfeir, T. Beetz, F. Wang, L. Huang, X.M.H. Huang, M. Huang, J. Hone, S. O'Brien, J.A. Misewich, T.F. Heinz, L. Wu, Y. Zhu, L.E. Brus, Science 312 (2006) 554.
[27] A. Jorio, A.P. Santos, H.B. Ribeiro, C. Fantini, M. Souza, J.P.M. Vieira, C.A. Furtado, J. Jiang, R. Saito, L. Balzano, D.E. Resasco, M.A. Pimenta, Phys. Rev. B 72 (2005) 075207.
[28] S. Giordani, S.D. Bergin, V. Nicolosi, S. Lebedkin, M.M. Kappes, W.J. Blau, J.N. Coleman, J. Phys. Chem. B 110 (2006) 15708.
[29] C. Fantini, A. Jorio, A.P. Santos, V.S.T. Peressinotto, M.A. Pimenta, Chem. Phys. Lett. 439 (2007) 138.
[30] D.A. Tsyboulski, E.L. Bakota, L.S. Witus, J.-D.R. Rocha, J.D. Hartgerink, R.B. Weisman, J. Amer. Chem. Soc. 130 (2008) 17134.
[31] S.D. Bergin, V. Nicolosi, H. Cathcart, M. Lotya, D. Rickard, Z. Sun, W.J. Blau, J.N. Coleman, J. Phys. Chem. C 112 (2008) 972.
[32] C. Fantini, J. Cassimiro, V.S.T. Peressinotto, F. Plentz, A.G. Souza Filho, C.A. Furtado, A.P. Santos, Chem. Phys. Lett. 473 (2009) 96.
[33] C.L. Kane, E.J. Mele, Phys. Rev. Lett. 90 (2003) 207401.
[34] K. Sato, R. Saito, J. Jiang, G. Dresselhaus, M.S. Dresselhaus, Phys. Rev. B 76 (2007) 195446.
[35] J. Jiang, R. Saito, Ge.G. Samsonidze, A. Jorio, S.G. Chou, G. Dresselhaus, M.S. Dresselhaus, Phys. Rev. B 75 (2007) 035407.
[36] V.N. Popov, New J. Phys. 6 (2004) 17.
[37] V.N. Popov, L. Henrard, Phys. Rev. B 70 (2004) 115407.
[38] Ge.G. Samsonidze, R. Saito, N. Kobayashi, A. Grneis, J. Jiang, A. Jorio, S.G. Chou, G. Dresselhaus, M.S. Dresselhaus, Appl. Phys. Lett. 85 (2004) 5703.
[39] C.D. Spataru, S. Ismail-Beigi, L.X. Benedict, S.G. Louie, Phys. Rev. Lett. 92 (2004) 077402.
[40] C.L. Kane, E.J. Mele, Phys. Rev. Lett. 93 (2004) 197402.
[41] P.T. Araujo, A. Jorio, M.S. Dresselhaus, K. Sato, R. Saito, Phys. Rev. Lett. 103 (2009) 146802.

[42] P. McEuen, Nanostructures, in: C. Kittel (Ed.), Introduction to Solid State Physics, Wiley, New York, 2005 (Chapter 18).
[43] K. Hata, D.N. Futaba, K. Mizuno, T. Namai, M. Yumura, S. Iijima, Science 306 (2004) 1362.
[44] D.N. Futaba, K. Hata, T. Yamada, K. Mizuno, M. Yumura, S. Iijima, Phys. Rev. Lett. 95 (2005) 056104.
[45] D.N. Futaba, K. Hata, T. Namai, T. Yamada, K. Mizuno, Y. Hayamizu, M. Yumura, S. Iijima, J. Phys. Chem. B 110 (15) (2006) 8035.
[46] D.N. Futaba, K. Hata, T. Yamada, T. Hiraoka, Y. Hayamizu, Y. Kakudate, O. Tanaike, H. Hatori, M. Yumura, S. Iijima, Nature Mater. 5 (2006) 987.
[47] A. Jorio, C. Fantini, M.A. Pimenta, R.B. Capaz, Ge.G. Samsonidze, G. Dresselhaus, M.S. Dresselhaus, J. Jiang, N. Kobayashi, A. Grneis, R. Saito, Phys. Rev. B 71 (2005) 075401.
[48] G.D. Mahan, Phys. Rev. B 65 (2002) 235402.
[49] M.J. Longhurst, N. Quirke, J. Chem. Phys. 124 (2006) 234708.
[50] L.A. Girifalco, M. Hodak, R.S. Lee, Phys. Rev. B 62 (2000) 13104.
[51] P.T. Araujo, C. Fantini, M.M. Lucchese, M.S. Dresselhaus, A. Jorio, Appl. Phys. Lett. 95 (2009) 261902.
[52] F. Wang, G. Dukovic, L.E. Brus, T.F. Heinz, Science 308 (2005) 838.
[53] J. Maultzsch, R. Pomraenke, S. Reich, E. Chang, D. Prezzi, A. Ruini, E. Molinari, M.S. Strano, C. Thomsen, C. Lienau, Phys. Rev. B 72 (2005) 241402(R).
[54] G. Dukovic, et al., Nanoletters 5 (2005) 2314.
[55] P.T. Araujo, A. Jorio, Phys. Stat. Sol. (b) 245 (2008) 2201.
[56] S.K. Doorn, P.T. Araujo, K. Hata, A. Jorio, Phys. Rev. B 78 (2008) 165408.
[57] Y. Miyauchi, R. Saito, K. Sato, Y. Ohno, S. Iwasaki, T. Mizutani, J. Jiang, S. Maruyama, Chem. Phys. Lett. 442 (2007) 394.
[58] V. Perebeinos, J. Tersoff, Ph. Avouris, Phys. Rev. Lett. 92 (2004) 257402.
[59] P.B.C. Pesce, P.T. Araujo, P. Nikolaev, S.K. Doorn, K. Hata, R. Saito, M.S. Dresselhaus, A. Jorio, Appl. Phys. Lett., in press, doi:10.1063/1.3297904.